

1 **From Precipitation to Prediction: Integrating**
2 **ConvLSTM Models for Comprehensive River Runoff**
3 **Forecasting**

4 **Florian Börgel¹, Sven Karsten¹, Karoline Rummel¹**

5 ¹Leibniz-Institute for Baltic Sea Research Warnemünde,

6 **Abstract**
 7 a

8 **Plain Language Summary**
 9 b

10 **1 Introduction**

11 River runoff is an important component of the global water cycle as it comprises
 12 about one third of the precipitation over land areas (Hagemann et al., 2020). In
 13 the context of climate change studies, river runoff is usually generated in two ways.
 14 First, river runoff as input for ocean models can be created using hydrological mod-
 15 els such as the Hydrological Discharge (HD) model (Hagemann et al., 2020). HD
 16 models calculates the water balance using hydrological processes (e.g. snow, glaciers,
 17 soil moisture, groundwater contribution). It represents a complex forecasting tool
 18 that uses underlying physical processes. A different approach would use data-based
 19 models that integrate statistical correction, using the land surface schemes of global
 20 or regional climate models.

21 The relatively recent emergence of machine learning (ML) models has offered differ-
 22 ent approaches to river runoff forecasting. Accurate runoff forecasting is crucial for
 23 effective water resources management, particularly over extended periods (W. Fang
 24 et al., 2019; Tan et al., 2018). Common approaches employ feed-forward artificial
 25 neural networks, support vector machines, adaptive neuro-fuzzy inference systems,
 26 and notably, Long Short-Term Memory (LSTM) neural networks that have gained
 27 traction for long-term hydrological forecasting due to their excellent performance
 28 (Ashrafi et al., 2017; L. Fang & Shao, 2022; Huang et al., 2014; Humphrey et al.,
 29 2016; Kratzert et al., 2018; Liu et al., 2020).

30 LSTM networks, first introduced by Hochreiter & Schmidhuber (1997) , are an evo-
 31 lution of the classical Recurrent Neural Networks (RNNs). Their structure enables
 32 them to learn long-term dependencies while avoiding the vanishing or exploding
 33 gradient problem. They have shown stability and efficacy in sequence-to-sequence
 34 predictions. However, a limitation of LSTMs is their inability to effectively capture
 35 two-dimensional structures, an area where Convolutional Neural Networks (CNNs)
 36 excel. Recognizing this limitation SHI et al. (2015) proposed a Convolutional LSTM
 37 (ConvLSTM) architecture, which combines the strengths of both LSTM and CNN.
 38 The ConvLSTM network has been proven useful for spatio-temporal applications
 39 such as precipitation nowcasting (SHI et al., 2015), flood forecasting (Moishin et al.,
 40 2021), and river runoff forecasting (Ha et al., 2021; Zhu et al., 2023).

41 In this work, we demonstrate that ConvLSTM networks are a reliable method for
 42 predicting multiple rivers simultaneously, using only atmospheric forcing, even in
 43 the absence of a fully functional hydrological model with a complex parameteriza-
 44 tion. We use the Baltic Sea catchment as an example to illustrate our approach.
 45 Although the methodology we propose is universally applicable across various geo-
 46 graphic regions, the Baltic Sea presents a challenge due to its unique hydrological
 47 characteristics, being nearly decoupled from the open ocean (see Figure). As a con-
 48 sequence, the salinity of the Baltic Sea is driven to a large part by freshwater supply
 49 from rivers. Freshwater enters the Baltic Sea through river runoff or positive net
 50 precipitation (precipitation minus evaporation) over the sea surface. The net precip-
 51 itation accounts for 11 % and the river input for 89 % of the total freshwater input
 52 (Meier & Döscher, 2002). Modelling the Baltic Sea is therefore to a large part the
 53 result of the quality of the river input, that is used for the simulation. This makes
 54 the accurate modeling of river runoff especially critical for simulations pertaining to
 55 the Baltic Sea.

56 In this work we will, we present a ConvLSTM architecture that is able to predict
 57 daily river runoff for 97 rivers across the Baltic Sea catchment. *mehr Fokus auf*
 58 *Neues?*

59 2 Implemented model architecture

60 2.1 The main idea

61 We assume that the runoff for a specific point in time of all N_r considered rivers,
 62 collected in the vector $\vec{R}^t \in \mathbb{R}^{N_r}$, can be accurately approximated by a functional
 63 $\vec{M}(\{X_k^t[x, y, \tau]\})$ of $k = 1, \dots, N_k$ atmospheric fields $X_k^t[x, y, \tau]$ that are known for the
 64 past $\tau = 1, \dots, N_\tau$ time instances, i.e.

$$\vec{R}^t = \vec{M}(\{X_k^t[x, y, \tau]\}) .$$

65 The fields are evaluated on a spatial domain $x = 1, \dots, N_x$ and $y = 1, \dots, N_y$ that is suf-
 66 ficiently large to capture all significant contributions to the modelled runoff.

67 We propose that this functional can be adequately represented by a combination
 68 of a ConvLSTM with a subsequent FC network as it is visualized in Figure 1 and
 69 described in detail in the following. In order to provide an overview, we will go
 70 through the main ingredients of this architecture one-by-one.

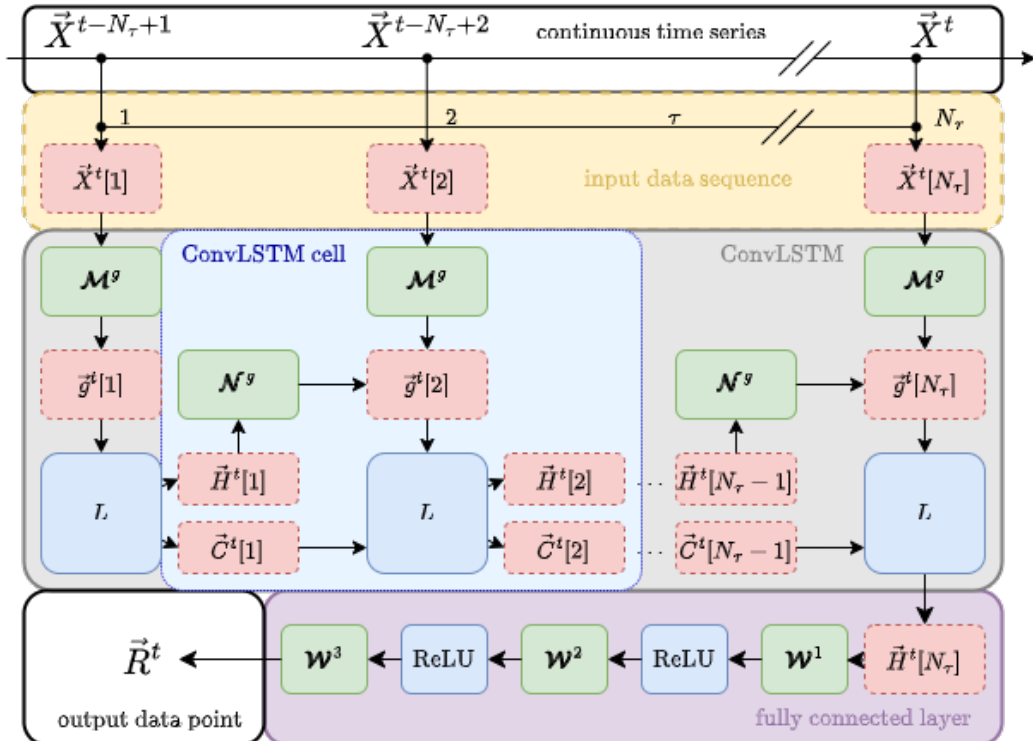


Figure 1

71 2.2 ConvLSTM network

72 **2.2.1 The LSTM approach**

73 Before turning to the convolutional LSTM, the simpler architecture of the plain
 74 LSTM is examined and should serve as a role model for the later consideration of
 75 the full ConvLSTM.

76 The Long Short-Term Memory (LSTM), a specialized form of Recurrent Neu-
 77 ral Networks (RNNs), is specifically tailored for modeling temporal sequences
 78 $\vec{X}^t[1], \dots \vec{X}^t[\tau], \dots \vec{X}^t[N_\tau]$ of N_τ input quantities $\vec{X}^t[\tau] = (X_k^t[\tau]) \in \mathbb{R}^{N_k}$. The se-
 79 quence is taken from a dataset given in form of a time series $\{\vec{X}^t\}$ and the endpoint
 80 should coincide with the specific element in the time series connected to time t ,
 81 i.e. $\vec{X}^t[N_\tau] \equiv \vec{X}^t$. The N_k is the number of used input “channels” and can, for exam-
 82 ple, represent different measurable quantities. Its unique design allows it to adeptly
 83 handle long-range dependencies, setting it apart from traditional RNNs in terms of
 84 accuracy (see Figure 2).

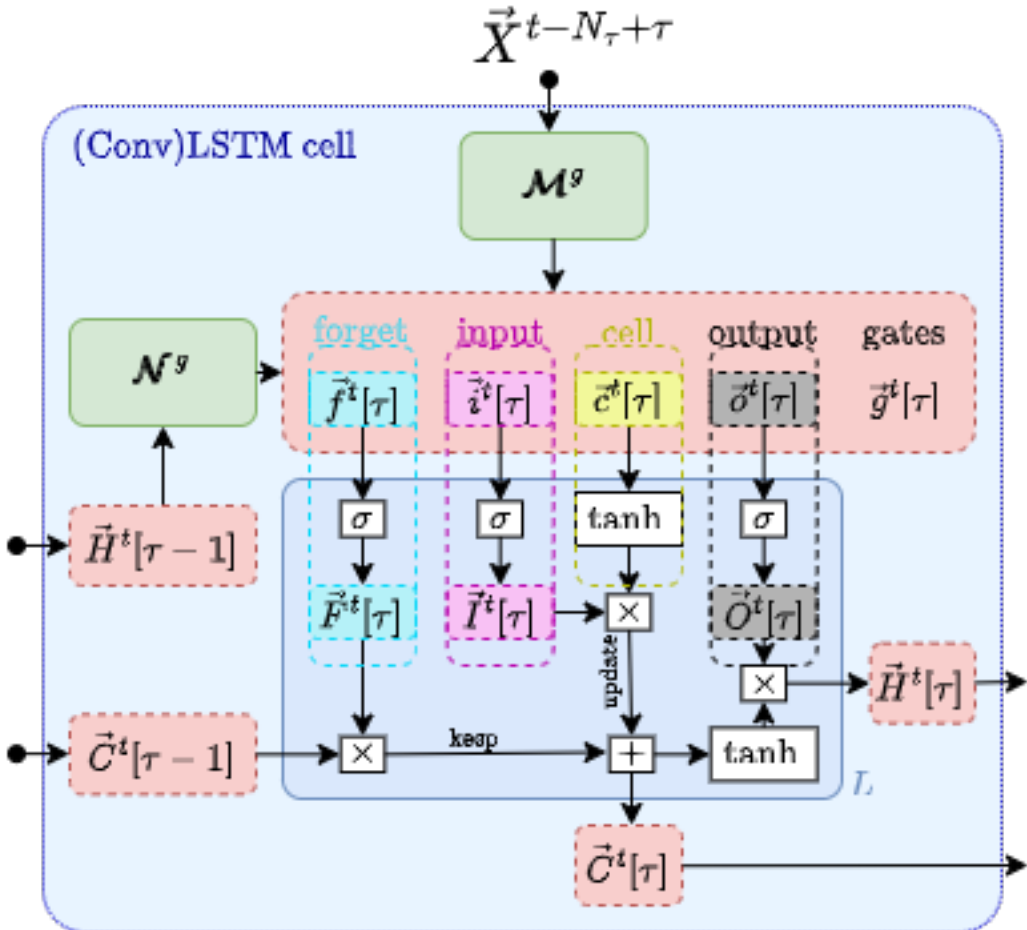


Figure 2: Inner structure of a Long Short-Term Memory Cell

85 This performance in modeling long-range dependencies has been validated in var-
 86 ious studies. The key component of the LSTM’s innovation is its memory cell,
 87 $\vec{C}^t[\tau] = (C_h^t[\tau]) \in \mathbb{R}^{N_h}$, which stores state information, also referred to as long-
 88 term memory. This state information complements the the so-called hidden state
 89 $\vec{H}^t[\tau] = (H_h^t[\tau]) \in \mathbb{R}^{N_h}$ vector, which is also known from simpler neural network

90 architectures. In case of the LSTM, the hidden state vector plays the role of the
 91 short-term memory. The cell state and the hidden state are vectors, where each element
 92 is associated with one of the so-called N_h hidden layers, labeled by h . These
 93 two state vectors are determined through several self-parameterized gates, all in the
 94 same vector space as $\vec{C}^t[\tau]$.

95 In particular, the forget gate $\vec{F}^t[\tau]$ defines the portion of the previous (long-term
 96 memory) cell state $\vec{C}^t[\tau - 1]$ that should be kept. The input gate $\vec{I}^t[\tau]$ controls the
 97 contribution of the current input that is used to update the long-term memory, $\vec{C}^t[\tau]$.
 98 The output gate $\vec{O}^t[\tau]$ then determines how much of this updated long-term memory
 99 contributes to the new (short-term memory) hidden state, $\vec{H}^t[\tau]$.

100 For a fixed point τ in the sequence, the action of a LSTM cell, i.e. the connection
 101 between the input $\vec{X}^t[\tau]$, the various gates and the state vectors, is mathematically
 102 given as follows.

First, the elements of the input sequence together with the hidden state are mapped
 onto auxiliary gate vectors, collectively denoted by $\vec{g}^t[\tau] = (g_h^t[\tau]) \in \mathbb{R}^{N_h}$, via

$$g_h^t[\tau] = \mathcal{M}_{hk}^g X_k^t[\tau] + \mathcal{N}_{hh'}^g H_{h'}^t[\tau - 1] + \mathcal{B}_h^g ,$$

103 where $g = i, f, o, c$ stands for the input, forget, output and cell-state gate, respectively
 104 and Einstein's summation convention is employed, i.e. indices that appear
 105 twice are summed over. The calligraphic symbols \mathcal{M}_{hk}^g , $\mathcal{N}_{hh'}^g$ and \mathcal{B}_h^g are the free
 106 parameters of the network that are optimized for the given problem during the
 107 training, which is at the heart of the any machine learning approach. The matrix
 108 $\mathcal{M}^g = (\mathcal{M}_{hk}^g) \in \mathbb{R}^{N_h \times N_h}$ can be interpreted as a Markovian-like contribution of
 109 the current input $\vec{X}^t[\tau]$ to the gates, whereas the $\mathcal{N}^g = (\mathcal{N}_{hh'}^g) \in \mathbb{R}^{N_h \times N_h}$ scales a
 110 non-Markovian part determined by the hidden state of the last sequence point $\tau - 1$.
 111 The vector $\vec{\mathcal{B}}^g = (\mathcal{B}_h^g) \in \mathbb{R}^{N_h}$ is a learnable bias. It should be stressed that these
 112 parameters do neither depend on t nor on τ and are thus optimized once for the
 113 complete dataset $\{\vec{X}^t\}$.

114 Note that this mapping is sometimes extended by a contribution to the $g_h^t[\tau]$ from
 115 the past cell state $\vec{C}^t[\tau - 1]$ (**XXX?**). Nevertheless, this mechanism called “peeping”
 116 is not further considered in this work.

For the sake of brevity, we write the mapping more compactly in matrix-vector form
 as

$$\vec{g}^t[\tau] = \mathcal{M}^g \vec{X}^t[\tau] + \mathcal{N}^g \vec{H}^t[\tau - 1] + \vec{\mathcal{B}}^g \quad (1)$$

117 Second, the actual gate vectors are computed by the core equations of the LSTM as
 118 proposed by (**XXX?**):

$$\begin{aligned} \vec{I}^t[\tau] &= \sigma(\vec{i}^t[\tau]) \\ \vec{F}^t[\tau] &= \sigma(\vec{f}^t[\tau]) \\ \vec{O}^t[\tau] &= \sigma(\vec{o}^t[\tau]) \\ \vec{C}^t[\tau] &= \vec{F}^t[\tau] \circ \vec{C}^t[\tau - 1] + \vec{I}^t[\tau] \circ \tanh(\vec{c}^t[\tau]) \\ \vec{H}^t[\tau] &= \vec{O}^t[\tau] \circ \tanh(\vec{C}^t[\tau]) , \end{aligned} \quad (2)$$

119 where σ denotes the logistic sigmoid function, \tanh is the hyperbolic tangent and
 120 the \circ stands for the Hadamard product (all applied in an element-wise fashion to the
 121 vectors). In the last two equations the role of the input, forget and output gates as
 122 described above becomes apparent.

123 The third step in a single layer LSTM (as employed for the work presented here)
 124 is then to provide the output of the current LSTM cell, i.e. $\vec{H}^t[\tau]$ and $\vec{C}^t[\tau]$, to

125 the subsequent LSTM cell that processes the next element $\vec{X}^t[\tau + 1]$ of the input
126 sequence.

127 The full action of the LSTM network up to the end of the sequence can therefore be
128 written as a nested function call

$$(\vec{H}^t[N_\tau], \vec{C}^t[N_\tau]) = L(\vec{X}^t[N_\tau], L(\vec{X}^t[N_\tau - 1], \dots L(\vec{X}^t[1], (\vec{H}^t[0], \vec{C}^t[0]) \dots))) , \quad (3)$$

129 where $L(\vec{X}^t[\tau], (\vec{H}^t[\tau - 1], \vec{C}^t[\tau - 1]))$ represents Equation 1 and Equation 2 and
130 the initial conditions are chosen as $\vec{H}^t[0] = \vec{C}^t[0] = 0$.

131 The final output $\vec{H}^t[N_\tau]$ and $\vec{C}^t[N_\tau]$ encode information on the full input sequence
132 ending at time t . This information has to be decoded to obtain useful information
133 via an appropriate subsequent layer, as it is described in the Section 2.3.

134 A significant advantage of this architecture is the memory cell's ability to retain gra-
135 dients. This mechanism addresses the vanishing gradient problem, where, as input
136 sequences elongate, the influence of initial stages becomes harder to capture, causing
137 gradients of early input points to approach zero. The LSTM's activation function,
138 inherently recurrent, mirrors the identity function with a consistent derivative of 1.0,
139 ensuring the gradient remains stable throughout backpropagation.

140 2.2.2 Combining LSTM with spatial convolution

141 Although the plain LSTM has high performance in handling temporal sequences
142 of point-like quantities it is not designed to recognize spatial features in sequences
143 of, e.g., two-dimensional maps. To address this limitation we employ a ConvLSTM
144 architecture as described in the following.

145 In this kind of network the elements of the input sequence are given as spatially
146 varying fields $\vec{X}^t[\tau] = (X_k^t[x, y, \tau]) \in \mathbb{R}^{N_k \times (N_x \times N_y)}$, where $x \in [1, N_x]$ and
147 $y \in [1, N_y]$ run over the horizontal and vertical dimensions of the map, respec-
148 tively. In order to enable the "learning" of spatial patterns, the free parameters
149 of the network are replaced by two-dimensional convolutional kernels $\mathcal{M}^g =$
150 $(\mathcal{M}_{hk}^g[\xi, \eta]) \in \mathbb{R}^{(N_h \times N_k) \times (N_\xi \times N_\eta)}$ and $\mathcal{N}^g =$
151 $(\mathcal{N}_{hh'}^g[\xi, \eta]) \in \mathbb{R}^{(N_h \times N_h) \times (N_\xi \times N_\eta)}$. The width and the height of the kernels are given by N_ξ and N_η , respectively and
152 $\xi \in [-(N_\xi - 1)/2, (N_\xi - 1)/2]$, $\eta \in [-(N_\eta - 1)/2, (N_\eta - 1)/2]$, where we assume odd
153 numbers for the kernel sizes.

The mapping from the input quantities to the gates is then given by a convolution
with these kernels

$$g_h^t[x, y, \tau] = \mathcal{M}_{hk}^g[\xi, \eta] X_k^t[x - \xi, y - \eta, \tau] + \mathcal{N}_{hh'}^g[\xi, \eta] H_{h'}^t[x - \xi, y - \eta, \tau - 1] + \mathcal{B}_h^g .$$

154 again with Einstein's convention imposed.

155 It becomes immediately apparent that in case of the ConvLSTM, gate and state
156 vectors must become vector fields ($\in \mathbb{R}^{N_h \times (N_x \times N_y)}$) as well. We can write this map-
157 ping in the same fashion as Equation 1 but with replacing the normal matrix-vector
158 multiplication by a convolution (denoted with $*$), i.e.

$$\vec{g}^t[\tau] = \mathcal{M}^g * \vec{X}^t[\tau] + \mathcal{N}^g * \vec{H}^t[\tau - 1] + \vec{\mathcal{B}}^g$$

159 The subsequent processing of the $\vec{g}^t[\tau]$ remains symbolically the same as presented
160 in Equation 2 but with all appearing quantities meaning standing now for vector
161 fields instead of simple vectors.

162 In summary, the ConvLSTM excels at processing tasks that demand a combined
163 understanding of spatial patterns and temporal sequences in data. It merges the

164 image-processing capabilities of Convolutional Neural Networks (CNNs) with the
 165 time-series modeling of Long Short-Term Memory (LSTM) networks.

166 2.3 Fully connected layer

167 As stated in Sec. Section 2.2.1, the final output $\vec{H}^t[N_\tau]$ and $\vec{C}^t[N_\tau]$ of the Con-
 168 vLSTM encode information on the full input sequence. In order to contract this
 169 information to the runoff vector \vec{R}^t representing the N_r rivers, we propose to sub-
 170 ject the final short-term memory (i.e. the hidden state $\vec{H}^t[N_\tau]$) to an additional FC
 171 network.

172 In particular, the dimensionality of the vector field $\vec{H}^t[N_\tau]$ is sequentially reduced
 173 by three nested FC layers, each connected to the other by the Rectified Linear Unit
 174 (ReLU), see Figure 1. Integrating over artificial degrees of freedom in a step-wise
 175 fashion has turned out to be beneficial ((**XXX?**)).

176 Spelled out in mathematics the runoff of the r -th river is then obtained via (using
 177 Einstein's convention)

$$R_r^t = \mathcal{W}_{rb}^3 \text{ReLU}(\mathcal{W}_{ba}^2 \text{ReLU}(\mathcal{W}_{ah}^1[x, y] H_h^t[x, y, N_\tau] + \mathcal{B}_a^1) + \mathcal{B}_b^2) + \mathcal{B}_r^3,$$

178 where $a = 1, \dots, N_a$ and $b = 1, \dots, N_b$ and $N_h \cdot N_x \cdot N_y > N_a > N_b > N_r$ in order
 179 to achieve the aforementioned step-by-step reduction of dimensionality. The weights
 180 \mathcal{W} and biases \mathcal{B} stand for parameters that are optimized during the training of the
 181 network.

In matrix-vector notation this can compactified to

$$\vec{R}^t = \mathcal{W}^3 \text{ReLU}(\mathcal{W}^2 \text{ReLU}(\mathcal{W}^1 \vec{H}^t[N_\tau] + \vec{\mathcal{B}}^1) + \vec{\mathcal{B}}^2) + \vec{\mathcal{B}}^3.$$

182 Combining this equation with Equation 3 provides finally an explicit formula for the
 183 initial assumption of modelling the runoff for time t as a functional of a sequence of
 184 atmospheric fields, i.e.

$$\begin{aligned} \vec{R}^t &= \vec{M}(\{X_k^t[x, y, \tau]\}) \\ &= \mathcal{W}^3 \text{ReLU}(\mathcal{W}^2 \text{ReLU}(\mathcal{W}^1 \vec{L}_H(\vec{X}^t[N_\tau], L(\vec{X}^t[N_\tau - 1], \dots, L(\vec{X}^t[1], (0, 0)) \dots)) + \vec{\mathcal{B}}^1) + \vec{\mathcal{B}}^2) + \vec{\mathcal{B}}^3, \end{aligned}$$

185 where the \vec{L}_H means that only the hidden state vector of the final ConvLSTM call
 186 is forwarded to the FC layer. In oder to make this model accurate the hyperpa-
 187 rameters have to be chosen reasonable and the free parameters are to be adjusted
 188 accordingly.

189 3 Technical details

190 3.1 Runoff data used for training

191 The runoff data covering the period 1979 to 2011 is based on an E-HYPE hindcast
 192 simulation that was forced by a regional downscaling of ERA-Interim (Dee et al.,
 193 2011) with RCA3 (“The rossby centre regional climate model RCA3,” n.d.) and im-
 194 plemented into NEMO-Nordic (Hordoir et al., 2019) as a mass flux. For the periods
 195 before (1961 to 1978) and after (2012 to 2018) additional spatial temporal correc-
 196 tions have been applied to the runoff data, and have therefore been ignored. For
 197 more information see Gröger et al. (2022) and references therein.

198 3.2 Atmospheric Forcing

199 The UERRA-HARMONIE regional reanalysis dataset was developed as part of
 200 the FP7 UERRA project (Uncertainties in Ensembles of Regional Re-Analyses,
 201 <http://www.uerra.eu/>). The UERRA-HARMONIE system represents a comprehen-
 202 sive, high-resolution reanalysis covering a wide range of essential climate variables.

This dataset encompasses data on air temperature, pressure, humidity, wind speed and direction, cloud cover, precipitation, albedo, surface heat fluxes, and radiation fluxes from January 1961 to July 2019. With a horizontal resolution of 11 km and analyses conducted at 00 UTC, 06 UTC, 12 UTC, and 18 UTC, it also provides hourly resolution forecast model data. UERRA-HARMONIE is accessible through the Copernicus Climate Data Store (CDS, <https://cds.climate.copernicus.eu/#!/home>), initially produced during the UERRA project and later transitioned to the Copernicus Climate Change Service (C3S, <https://climate.copernicus.eu/copernicus-regionalreanalysis-europe>).

3.3 Ocean Model

To simulate the Baltic Sea, we use a coupled 3-dimensional ocean model Baltic Sea, called the Modular Ocean Model (MOM). This model uses a finite-difference method to solve the full set of primitive equations to calculate the motion of water and the transport of heat and salt. The K-profile parameterization (KPP) was used as turbulence closure scheme. The model's western boundary opens into the Skagerrak and connects the Baltic Sea to the North Sea. The maximum depth was set at 264 meters. A more detailed description of the setup can be found in (Gröger et al., 2022).

3.4 Neural network hyper parameters

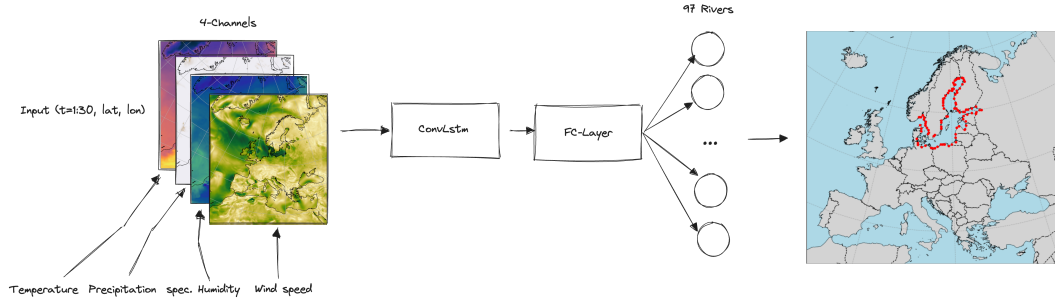


Figure 3: Schematic structure of the ConvLSTM implementation for river runoff forecasting.

For the computation we use the following set of hyper parameters:

Table 1: Hyperparameters

Parameter name	Parameter size
Channel size	4
Num. hidden layer	9
Num. timesteps	30
Conv. Kernelsize	(7,7)
Num. ConvLSTM layers	1
Batch size	50
Learning Rate	1e-3 with CosineAnnealing

As input the model receives 30 days of atmospheric surface fields temperature T , precipitation P , specific humidity Q and wind speed W , with a daily resolution to predict the river runoff R at the time step $\Delta t + 1$, which can be summarized as

$$R_{\Delta t+1} = f(T_{t-30:t}, P_{t-30:t}, Q_{t-30:t}, W_{t-30:t})$$

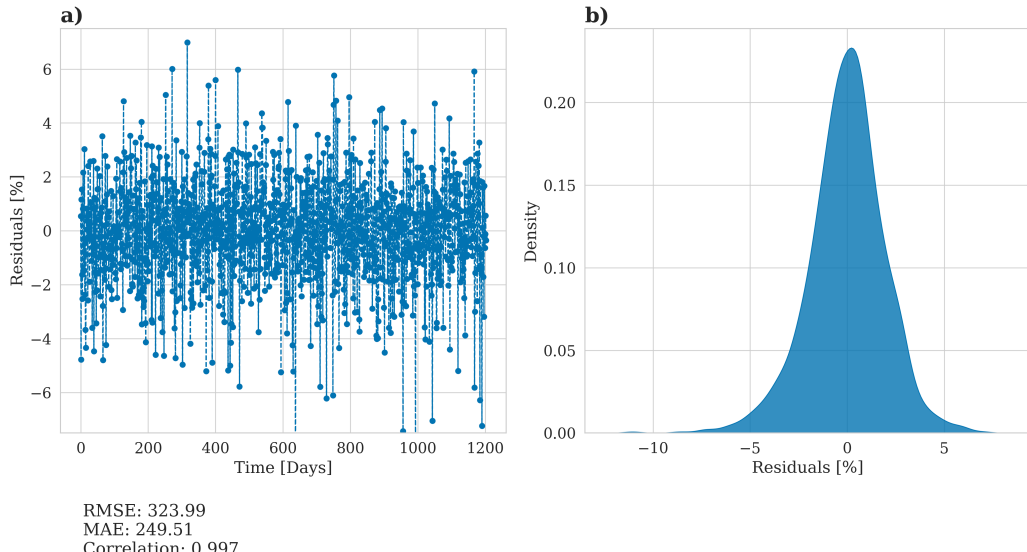
with f being a function maps the 30 days of daily atmospheric surface fields data to the predicted river runoff.

The choice of atmospheric fields was based on the implemented river runoff calculation in the atmospheric model COSMO-CLM which uses these four fields to calculate an river runoff estimate.

4 Results

The model was trained with daily data for the period 1979 to 2011, as this period represents the only period of E-HYPE without further bias correction applied to the runoff to match observations. The data was divided into randomly chosen splits of 80% training data, 10% validation data to evaluate the performance of the model during training, and 10% training data which is finally used to evaluate the performance of the model after training. The model was trained for 400 epochs and the model weights with the lowest mean squared error during training have been stored.

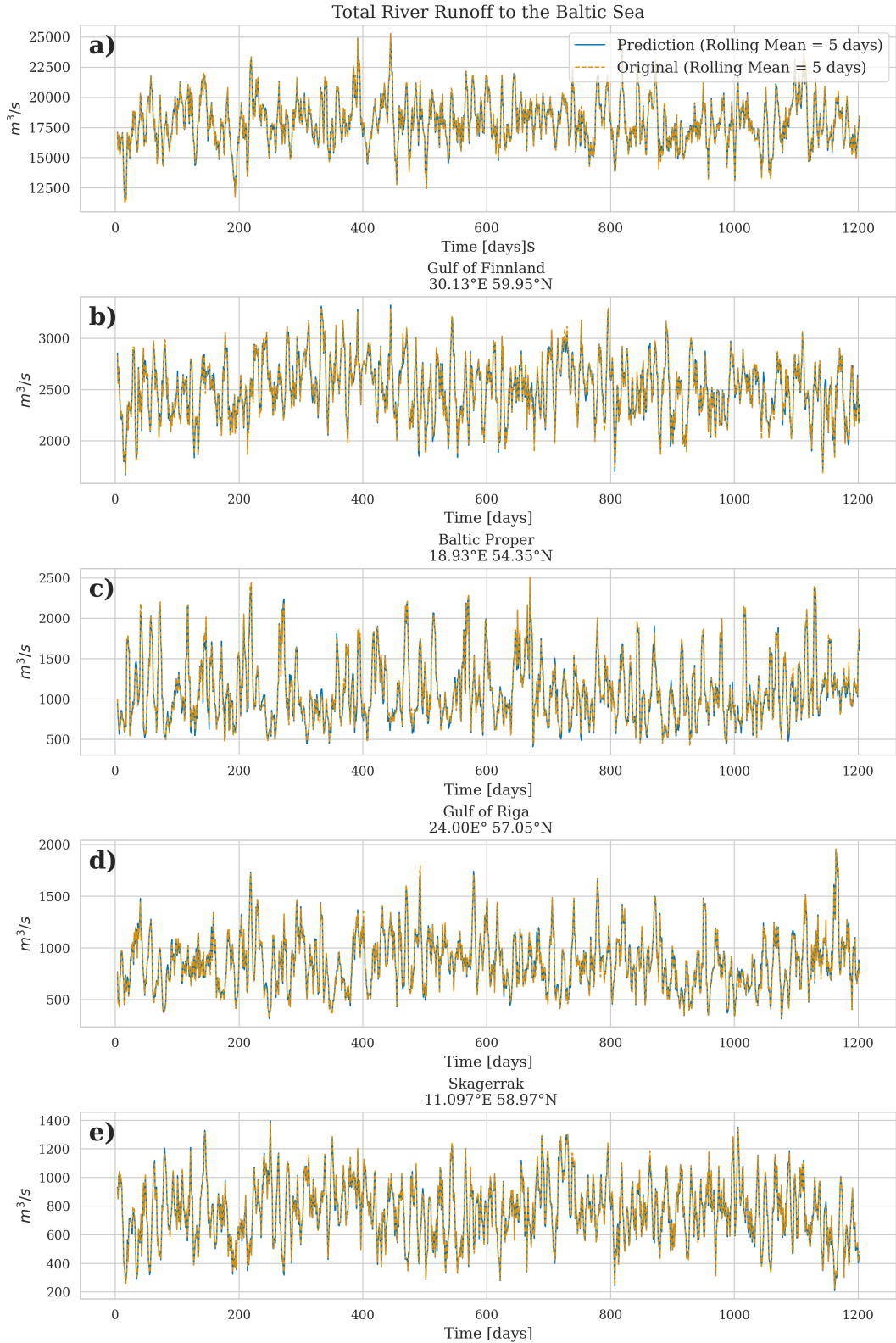
The accuracy of the model is displayed in Figure ?@fig-statistical-evaluationNN. As mention above for evaluation, the test dataset was utilized. The left panel (Figure ?@fig-statistical-evaluationNN a)) illustrates the relative prediction error in relation to the original E-HYPE data, indicating that, on daily timescales, the model can predict river runoff with an accuracy of $\pm 5\%$. The overall correlation is 0.997 with the resulting error metrics yielding a RMSE of $323.99 \text{ m}^3/\text{s}$ and MAE of $249.51 \text{ m}^3/\text{s}$. While the model's performance is satisfactory, the discrepancies between the actual values and the predictions could partly be attributed to the use of a different atmospheric dataset than the one originally used to drive the E-HYPE model. However, by applying a rolling mean with a 5-day window, the prediction error is reduced to less than 1%, which is acceptable for the purposes of climate modeling. Lastly, the right panel demonstrates that the distribution of residuals follows a Gaussian shape, suggesting that our model does not exhibit bias by systematically over or underestimating river runoff values.



254

In the following we will now address the overall performance of the total river runoff while also zooming in on the four largest rivers entering the Baltic Sea. @fig-PerformanceNeuralNetworkRunoff shows the predicted and the original river runoff using the test dataset. The predicted total river runoff for the Baltic Sea is closely matching the original data (@fig-PerformanceNeuralNetworkRunoff a). Zooming in

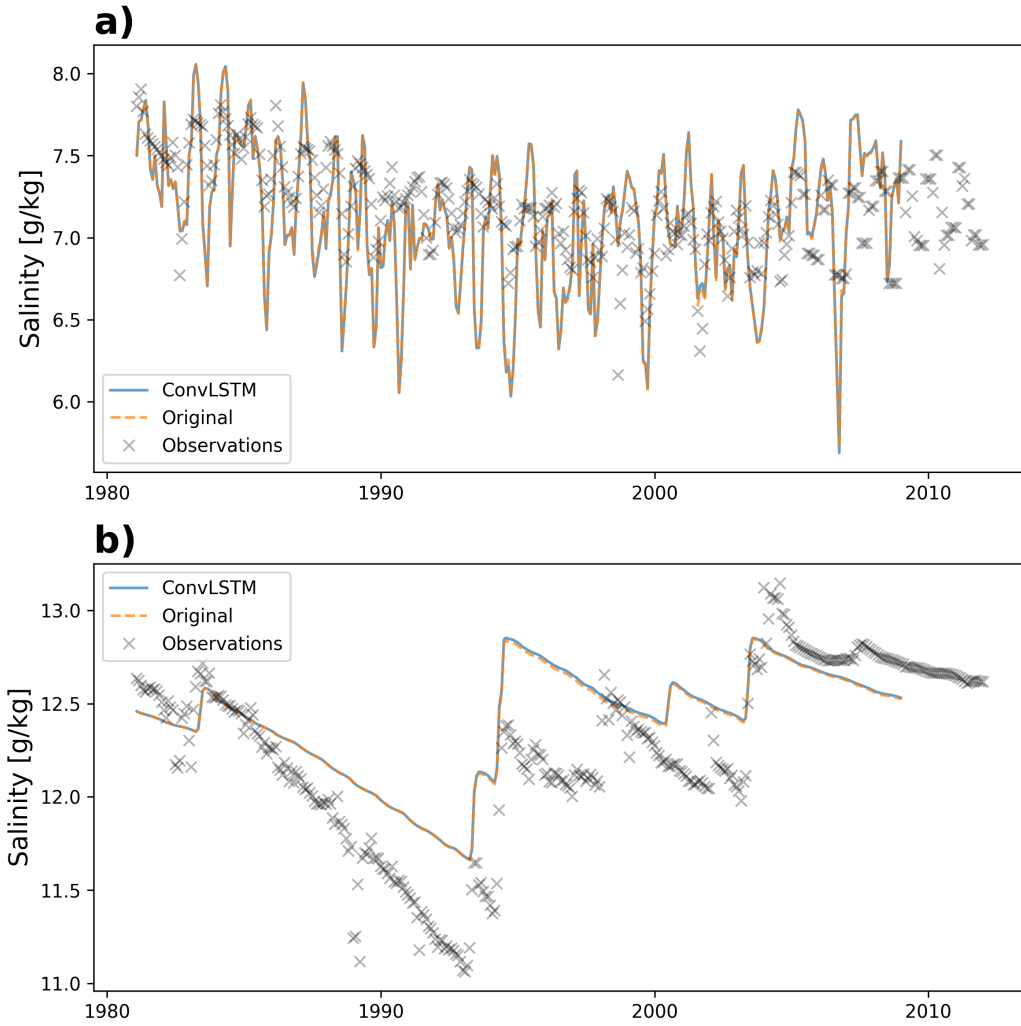
260 on the largest individual rivers (@fig-PerformanceNeuralNetworkRunoff b-e) it can
 261 be seen that that also the prediction of the individual rivers is close to the original
 262 data.



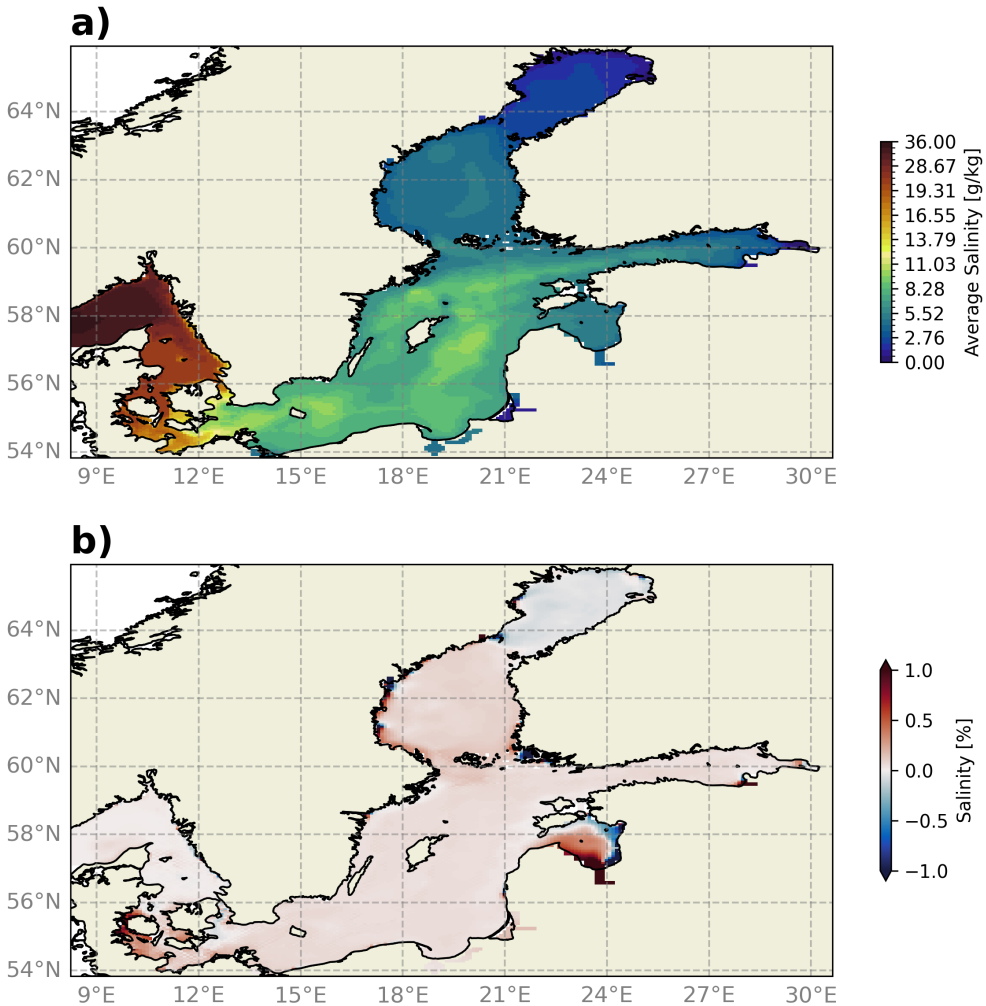
263

264 Lastly, we evaluated the performance of the runoff model by incorporating the pre-
 265 dicted river runoff as runoff forcing into the ocean model MOM5. This provides a

robust validation of the runoff model against more complex real world conditions. This allows us to ensure that the predictions accurately reflect the impact of the river discharge on the ocean dynamics, validating the temporal and spatial variability of the the river discharge. ?@fig-by15 shows the salinity comparison between the original E-HYPE river runoff and the predicted river runoff at BY15 - a central stations in the Baltic Sea. It can be seen that the model simulation using the predicted river runoff by the ConvLSTM is closely mirroring the control simulation. The upper panel (?@fig-by15 a) shows the surface salinity, representing the high-frequency variations in the salinity, which is heavily affected by river runoff. The lower panel (?@fig-by15 b) shows the bottom salinity which can be viewed as a low-pass filter in the Baltic Sea, which is also closely mirrored by the ConvLSTM predictions.



The final evaluation of the ConvLSTM model concentrates on the spatial accuracy of river runoff predictions. Figure xxx a) shows the vertically averaged salinity for the period 1981 to 2011 in the reference simulation. It highlights the strong horizontal gradients and complex topographic features in the Baltic Sea, as evidenced by salinity variations in deeper waters, captured by the vertical integration. Figure 4b compares these results by showing the percentage difference in vertically averaged salinity between the ConvLSTM simulation and the reference simulation. Overall, the differences remain below 1%, except near a river mouth in the Gulf of Riga (22-24°E, 56.5-58.5°N for orientation), where the difference is approximately 1%.



288

5 Discussion

With the increasing demand of decision makers for regional climate projections, that allow to quantify regional climate change impacts, the availability of precise hydrological forecasting becomes invaluable. The quality of a projection for a coastal sea such as the Baltic Sea is too large parts based on the quality of the hydrological conditions. In this work we analyze the implementation of Convolutional Long Short-Term Memory (ConvLSTM) networks for predicting river runoff, highlighting its potential to enhance river runoff forecasting across different coastal seas. Given the unique hydrological characteristics of the Baltic Sea, largely influenced by its limited connection to the open ocean and significant freshwater input from surrounding rivers, the region presents a critical case for the application of sophisticated forecasting models.

The transition from traditional hydrological models to machine learning approaches, such as the ConvLSTM model, offers significant advantages. The ConvLSTM can be seamlessly integrated into regional climate models, allowing for the real-time computation of river runoff while performing climate projections. While the initial training of the model requires substantial computational resources, it remains less intensive than running comprehensive hydrological models. Furthermore, once trained, the ConvLSTM model is computationally efficient during inference, ensuring enhanced forecasting capabilities without significantly increasing computational demands.

309 While the ConvLSTM represents an advancement for the climate community, given
 310 that running and tuning traditional hydrological models demands extensive exper-
 311 tise, models like E-HYPE maintain an essential role. They provide a comprehensive
 312 dataset that helps to train our ConvLSTM model effectively. This robust training
 313 enables the machine learning models to achieve highly accurate predictive weights.
 314 Thus, rather than rendering traditional methods obsolete, the integration of machine
 315 learning models builds upon and enhances the foundational data provided by them.

316 The robust performance of the ConvLSTM model in simulating river runoff and
 317 its possible effective integration into regional climate models pave the way for a
 318 multitude of new storyline simulations. Hence, we can now explore various “what-
 319 if” scenarios more reliably, under the assumption that the model weights attained
 320 during training are robust.

321 In summary, we showed that the ConvLSTM model demonstrated robust perfor-
 322 mance in forecasting river runoff across 97 rivers entering the Baltic Sea. Trained
 323 on data from 1979 to 2011, the model achieved an impressive daily prediction accu-
 324 racy of $\pm 5\%$. This capability to generate accurate and detailed simulations enables
 325 to examine the potential impacts of different climate scenarios. Such precision in
 326 forecasting and scenario testing is crucial for crafting effective water resource man-
 327 agement strategies and adapting to the changing climate.

328 Ultimately, the integration of ConvLSTM into regional climate models represents a
 329 significant step forward in our ability to understand and predict the complex dynam-
 330 ics of river systems and their impact on regional climate systems.

331 **6 Acknowledgments**

332 Phasellus interdum tincidunt ex, a euismod massa pulvinar at. Ut fringilla ut nisi
 333 nec volutpat. Morbi imperdiet congue tincidunt. Vivamus eget rutrum purus. Etiam
 334 et pretium justo. Donec et egestas sem. Donec molestie ex sit amet viverra egestas.
 335 Nullam justo nulla, fringilla at iaculis in, posuere non mauris. Ut eget imperdiet elit.

336 **7 Open research**

337 Phasellus interdum tincidunt ex, a euismod massa pulvinar at. Ut fringilla ut nisi
 338 nec volutpat. Morbi imperdiet congue tincidunt. Vivamus eget rutrum purus. Etiam
 339 et pretium justo. Donec et egestas sem. Donec molestie ex sit amet viverra egestas.
 340 Nullam justo nulla, fringilla at iaculis in, posuere non mauris. Ut eget imperdiet elit.

341 **References**

- 342 Ashrafi, M., Chua, L. H. C., Quek, C., & Qin, X. (2017). A fully-online neuro-fuzzy
 343 model for flow forecasting in basins with limited data. *Journal of Hydrology*, 545,
 344 424–435.
- 345 Dee, D. P., Uppala, S. M., Simmons, A. J., Berrisford, P., Poli, P., Kobayashi, S., et
 346 al. (2011). The ERA-Interim reanalysis: configuration and performance of the
 347 data assimilation system. *Quarterly Journal of the Royal Meteorological Society*,
 348 137(656), 553–597. <https://doi.org/10.1002/qj.828>
- 349 Fang, L., & Shao, D. (2022). Application of long short-term memory (LSTM) on the
 350 prediction of rainfall-runoff in karst area. *Frontiers in Physics*, 9, 790687.
- 351 Fang, W., Huang, S., Ren, K., Huang, Q., Huang, G., Cheng, G., & Li, K. (2019).
 352 Examining the applicability of different sampling techniques in the development
 353 of decomposition-based streamflow forecasting models. *Journal of Hydrology*, 568,
 354 534–550. <https://doi.org/10.1016/j.jhydrol.2018.11.020>
- 355 Gröger, M., Placke, M., Meier, M., Börgel, F., Brunnabend, S.-E., Dutheil, C., et
 356 al. (2022). *The Baltic Sea model inter-comparison project BMIP – a platform
 357 for model development, evaluation, and uncertainty assessment*. Retrieved from
<https://gmd.copernicus.org/preprints/gmd-2022-160/>

- 359 Ha, S., Liu, D., & Mu, L. (2021). Prediction of Yangtze River streamflow based
 360 on deep learning neural network with El Niño–Southern Oscillation. *Scientific
 361 Reports*, 11(1), 11738. <https://doi.org/10.1038/s41598-021-90964-3>
- 362 Hagemann, S., Stacke, T., & Ho-Hagemann, H. T. M. (2020). High Resolution Dis-
 363 charge Simulations Over Europe and the Baltic Sea Catchment. *Frontiers in
 364 Earth Science*, 8. <https://doi.org/10.3389/feart.2020.00012>
- 365 Hochreiter, S., & Schmidhuber, J. (1997). Long short-term memory. *Neural Compu-
 366 tation*, 9(8), 1735–1780.
- 367 Hordoir, R., Axell, L., Höglund, A., Dieterich, C., Fransner, F., Gröger, M., et al.
 368 (2019). Nemo-nordic 1.0: A NEMO-based ocean model for the baltic and north
 369 seas – research and operational applications. *Geoscientific Model Development*,
 370 12(1), 363–386. <https://doi.org/10.5194/gmd-12-363-2019>
- 371 Huang, S., Chang, J., Huang, Q., & Chen, Y. (2014). Monthly streamflow prediction
 372 using modified EMD-based support vector machine. *Journal of Hydrology*, 511,
 373 764–775.
- 374 Humphrey, G. B., Gibbs, M. S., Dandy, G. C., & Maier, H. R. (2016). A hybrid
 375 approach to monthly streamflow forecasting: Integrating hydrological model
 376 outputs into a bayesian artificial neural network. *Journal of Hydrology*, 540,
 377 623–640.
- 378 Kratzert, F., Klotz, D., Brenner, C., Schulz, K., & Herrnegger, M. (2018). Rainfall–
 379 runoff modelling using long short-term memory (LSTM) networks. *Hydrology
 380 and Earth System Sciences*, 22(11), 6005–6022.
- 381 Liu, D., Jiang, W., Mu, L., & Wang, S. (2020). Streamflow prediction using deep
 382 learning neural network: Case study of yangtze river. *IEEE Access*, 8, 90069–
 383 90086.
- 384 Meier, H. M., & Döscher, R. (2002). Simulated water and heat cycles of the baltic
 385 sea using a 3D coupled atmosphere–ice–ocean model. *Boreal Environment Re-
 386 search*, 7(4), 327.
- 387 Moishin, M., Deo, R. C., Prasad, R., Raj, N., & Abdulla, S. (2021). Designing deep-
 388 based learning flood forecast model with ConvLSTM hybrid algorithm. *IEEE
 389 Access*, 9, 50982–50993.
- 390 SHI, X., Chen, Z., Wang, H., Yeung, D.-Y., Wong, W., & WOO, W. (2015). Con-
 391 volutional LSTM Network: A Machine Learning Approach for Precipitation
 392 Nowcasting. In *Advances in Neural Information Processing Systems* (Vol. 28).
 393 Curran Associates, Inc. Retrieved from <https://proceedings.neurips.cc/paper/2015/hash/07563a3fe3bbe7e3ba84431ad9d055af-Abstract.html>
- 394 Tan, Q.-F., Lei, X.-H., Wang, X., Wang, H., Wen, X., Ji, Y., & Kang, A.-Q. (2018).
 395 An adaptive middle and long-term runoff forecast model using EEMD-ANN hy-
 396 brid approach. *Journal of Hydrology*, 567, 767–780. <https://doi.org/10.1016/j.jhydrol.2018.01.015>
- 397 The rossby centre regional climate model RCA3: Model description and perfor-
 398 mance - tellus a: Dynamic meteorology and oceanography. (n.d.). Retrieved
 399 from <https://a.tellusjournals.se/articles/10.1111/j.1600-0870.2010.00478.x>
- 400 Zhu, S., Wei, J., Zhang, H., Xu, Y., & Qin, H. (2023). Spatiotemporal deep learning
 401 rainfall-runoff forecasting combined with remote sensing precipitation products in
 402 large scale basins. *Journal of Hydrology*, 616, 128727.
- 403